nature chemistry

ARTICLES

https://doi.org/10.1038/s41557-020-0507-3

Check for updates

Tracking the ultraviolet-induced photochemistry of thiophenone during and after ultrafast ring opening

Shashank Pathak[1,16], Lea M. Ibele[2,16], Rebecca Boll[3], Carlo Callegari[4], Alexander Demidovich[4], Benjamin Erk[5], Raimund Feifel[6], Ruaridh Forbes[7], Michele Di Fraia[4], Luca Giannessi[4,8], Christopher S. Hansen[9], David M. P. Holland[10], Rebecca A. Ingle[11], Robert Mason[12], Oksana Plekan[4], Kevin C. Prince[4,13], Arnaud Rouzée[14], Richard J. Squibb[6], Jan Tross[1], Michael N. R. Ashfold[15] ✉, Basile F. E. Curchod[2] ✉ and Daniel Rolles[1] ✉

Photoinduced isomerization reactions lie at the heart of many chemical processes in nature. The mechanisms of such reactions are determined by a delicate interplay of coupled electronic and nuclear dynamics occurring on the femtosecond scale, followed by the slower redistribution of energy into different vibrational degrees of freedom. Here we apply time-resolved photoelectron spectroscopy with a seeded extreme ultraviolet free-electron laser to trace the ultrafast ring opening of gas-phase thiophenone molecules following ultraviolet photoexcitation. When combined with ab initio electronic structure and molecular dynamics calculations of the excited- and ground-state molecules, the results provide insights into both the electronic and nuclear dynamics of this fundamental class of reactions. The initial ring opening and non-adiabatic coupling to the electronic ground state are shown to be driven by ballistic S–C bond extension and to be complete within 350 fs. Theory and experiment also enable visualization of the rich ground-state dynamics that involve the formation of, and interconversion between, ring-opened isomers and the cyclic structure, as well as fragmentation over much longer timescales.

Recent advances in time-resolved experimental techniques and in computational methods for treating (coupled) electronic and nuclear dynamics are revolutionizing the field of ultrafast photochemistry, enabling direct probing of evolving molecular structures with unprecedented structural and temporal resolution[1–8]. Such studies provide the ultimate test of our knowledge and understanding of light-initiated chemistry. Photoinduced ring-opening/closing reactions play a crucial role in many key processes in nature, such as the synthesis of natural products (for example, the synthesis of previtamin D_3 by sunlight) and are currently attracting interest as molecular and biomolecular switches for photocontrolled switching of enzyme activity, optical data storage, the modulation of energy and electron transfer processes[9,10] and potential medical applications[11]. Ring-opening reactions featured prominently in the development of the Woodward–Hoffmann rules, which help rationalize the mechanisms and outcomes of pericyclic reactions. It is now recognized that photoinduced isomerization (including ring-opening) reactions are governed by strong non-adiabatic coupling between multiple electronic states of the molecule via conical intersections, which represent a breakdown of the Born–Oppenheimer approximation[5,12].

The photoinduced ring opening of the polyene 1,3-cyclohexadiene[13] is widely employed as a model system for benchmarking and validating ultrafast methods such as ultrafast X-ray[1,7,8] and electron[6] diffraction, femtosecond transient X-ray absorption[4] and fragmentation[14], and time-resolved photoelectron spectroscopy (TRPES)[15,16]. However, few other photoinduced ring-opening reactions have been probed so thoroughly and, of these, even fewer have provided a comprehensive picture of the reaction dynamics on both the excited and ground (S_0) state potential energy surfaces (PESs).

Here we report a combined theoretical and experimental study of the UV photoinduced ring opening of a prototypical heterocyclic molecule, 2(5H)-thiophenone (C_4H_4OS, henceforth thiophenone; see Fig. 1). Heterocyclic compounds are fundamental building blocks in the synthesis of many organic compounds. Studying these 'single units' may help in validating the (necessarily more complex and less resolvable) photochemistry of ever-larger molecules. The study is conducted in the gas phase (that is, under collision-free conditions) and thus reveals information on the purely intramolecular relaxation pathways, without the solvation effects present in previous matrix-isolation[17] and liquid-phase[18] studies of this system. Theory and experiment combine to afford detailed insights into both the mechanism and timescale of the initial ring-opening process and the subsequent evolution of the vibrationally excited ground-state photoproducts.

[1]J.R. Macdonald Laboratory, Department of Physics, Kansas State University, Manhattan, KS, USA. [2]Department of Chemistry, Durham University, Durham, UK. [3]European XFEL, Schenefeld, Germany. [4]Elettra-Sincrotrone Trieste S.C.p.A., Trieste, Italy. [5]Deutsches Elektronen-Synchrotron, Hamburg, Germany. [6]Department of Physics, University of Gothenburg, Gothenburg, Sweden. [7]Stanford PULSE Institute, SLAC National Accelerator Laboratory, Menlo Park, CA, USA. [8]Istituto Nazionale di Fisica Nucleare, Laboratori Nazionali di Frascati, Frascati, Italy. [9]School of Chemistry, University of New South Wales, Sydney, New South Wales, Australia. [10]Daresbury Laboratory, Warrington, UK. [11]Department of Chemistry, University College London, London, UK. [12]Department of Chemistry, University of Oxford, Oxford, UK. [13]Centre for Translational Atomaterials, Swinburne University of Technology, Melbourne, Victoria, Australia. [14]Max-Born-Institut, Berlin, Germany. [15]School of Chemistry, University of Bristol, Bristol, UK. [16]These authors contributed equally: Shashank Pathak, Lea M. Ibele. ✉e-mail: mike.ashfold@bristol.ac.uk; basile.f.curchod@durham.ac.uk; rolles@phys.ksu.edu

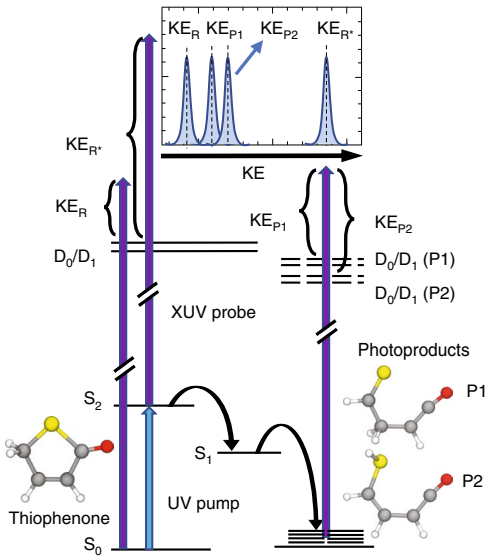

Fig. 1 | Schematic of the UV excitation, ring opening and photoionization of thiophenone. The molecule is photoexcited from its ring-closed ground state (S_0) to an electronically excited state (S_2). It evolves through an optically dark excited state (S_1) back to the (vibrationally excited) S_0 state of several possible reaction products (P1, P2 and so on). The XUV probe photon energy is sufficient to ionize thiophenone and all reaction products from both ground and excited states into several ionic final states (D_0, D_1 and so on). The time-evolving electron kinetic energy (KE) spectrum (top) thus consists of contributions from the ground and excited states of thiophenone (denoted as R and R*, respectively) and from the different products. In the depictions of the molecular geometry, carbon atoms are shown in grey, hydrogen in white, oxygen in red and sulfur in yellow.

The experimental study employs the extreme UV (XUV) radiation provided by the free-electron laser (FEL) FERMI[19]. TRPES[20,21] is sensitive to both electronic and structural dynamics, which is essential for any full understanding of the coupled electronic and nuclear dynamics that govern most photoinduced reactions. TRPES also allows access to so-called 'dark' states that may not be amenable to study by transient absorption methods. XUV probe pulses (from an FEL or a high harmonic generation source) are sufficiently energetic to ionize molecules in the electronic ground state (S_0), thereby overcoming a long-recognized shortcoming of previous TRPES studies that employed lower energy (UV) photons and were thus unable to reveal the ultimate structural dynamics following transfer from an electronically excited state to the ground state[16,22–26]. FERMI is a seeded FEL[19,27], in which an external laser is used to initiate the XUV generation, offering the advantages of (1) a narrower photon energy bandwidth (that is, higher energy resolution) and higher stability compared to FELs based on self-amplified spontaneous emission (SASE), and (2) higher pulse energies and photon fluxes as compared to monochromatized XUV sources based on high harmonic generation.

In the present experiment, gas-phase thiophenone molecules are excited to the optically bright S_2 electronic state by a UV pulse ($\lambda \approx 265$ nm). The excited molecules evolve through one or more conical intersections at progressively greater C–S bond separations en route back to the S_0-state PES, where they can adopt the original closed-ring or one of several possible open-ring geometries[18,28], some of which are sketched in Fig. 1. The evolving wavepacket and the formation of open- and closed-ring photoproducts are probed by ionizing the molecule with a time-delayed 19.24 eV ($\lambda = 64.44$ nm) XUV pulse. Time-dependent photoelectron time-of-flight spectra are recorded as a function of the time delay (Δt) between the UV and FEL pulses using a magnetic bottle spectrometer (see Methods and Supplementary Fig. 1). The FEL photon energy is deliberately chosen to be well above the first ionization potential (IP) of the ground-state molecule (~9.7 eV)[29] but below the IP of the helium carrier gas, ensuring that the electronic character of the target molecule can be traced throughout the complete structural evolution with only minimum background signal from the carrier gas. The experimental results are complemented by high-level ab initio electronic structure and molecular dynamics calculations of both excited- and ground-state molecules. These calculations afford insight into the ultrafast electronic de-excitation that accompanies ring opening and the subsequent interconversion between different isomeric forms of the highly vibrationally excited ground-state photoproducts.

Results and discussion

Experimental results. The experiment measures electron time-of-flight spectra of thiophenone as a function of Δt. The spectra are converted to electron kinetic energy spectra and then, by energy conservation, into spectra of the valence binding energies (see Methods). Figure 2a shows such spectra in the form of a two-dimensional plot of electron yield as functions of binding energy (BE) and Δt. The dominant feature, at BE ≈ 9.7 eV, is due to photoionization of the 'cold' (that is, non-excited) closed-ring S_0-state thiophenone molecule[29]. This peak is depleted by ~20% for positive Δt, as shown in Fig. 2b (red circles), confirming excitation of ground-state molecules by the UV pulse. A fit to the delay-dependent yield of photoelectrons originating from S_0-state parent molecules yields an upper limit for the temporal instrument response function of $\sigma = 72 \pm 8$ fs. Figure 2a reveals photoelectrons with BEs as low as ~5 eV at the shortest positive Δt. The prompt appearance and subsequent decay of this contribution is also emphasized in Fig. 2b, which shows a Gaussian-shaped transient signal with $\sigma = 76 \pm 6$ fs (blue triangles). With increasing delay, the signal at BE ≈ 5 eV fades, and the peak intensity shifts towards higher BE. As Fig. 2c shows, the peak in the intensity versus Δt transient obtained by taking contiguous 0.6 eV-wide slices for BE ≥ 5.3 eV shifts to progressively later Δt with increasing BE, and the transients gain an increasingly obvious tail.

The thiophenone cation has close-lying ground (D_0) and first excited (D_1) states at a vertical IP (IP_{vert}) of ~9.7 eV and higher excited states at IP_{vert} values of 10.58 eV (D_2), 12.25 eV (D_3) and 14.1 eV (D_4)[29]. Given the present pump photon energy of 4.67 eV, the signal appearing at a binding energy of ~5 eV at $\Delta t \approx 0$ is readily attributed to vertical ionization of photoexcited molecules in the S_2 state to the (unresolved) D_0 and D_1 states. Ionization to the D_1 state is strongly disfavoured due to selection rules, as discussed in Section 2.3 of the Supplementary Information. The evolution of the signal at BE ≈ 5 eV, the peak shift towards higher BE at later Δt and the more intense tail in the Δt traces for higher BE slices all reflect the complex evolution of the photoprepared wavepacket, which the accompanying theory shows involves ultrafast depopulation of the S_2 state to yield 'hot', that is, highly vibrationally excited, S_0 (henceforth $S_0^{\#}$) molecules (revealed by the teal green stripe in Fig. 2a at BE ≈ 9 eV). Note that any photoelectrons arising from ionization of $S_0^{\#}$ molecules to excited D_n ($n > 1$) cation states are likely to appear at BE > 10 eV (see extended spectrum in Supplementary Fig. 2) and thus do not affect the discussion that follows.

Calculations of decay pathways and excited-state dynamics. To interpret the dynamics revealed in the TRPES spectra, the lowest-lying PESs of thiophenone were computed and different critical points were located using SA(4)-CASSCF(10/8) calculations, and their energies further refined using XMS(4)-CASPT2(10/8) (see Computational details for more information). The Franck–Condon (FC) geometry corresponds to the equilibrium structure of

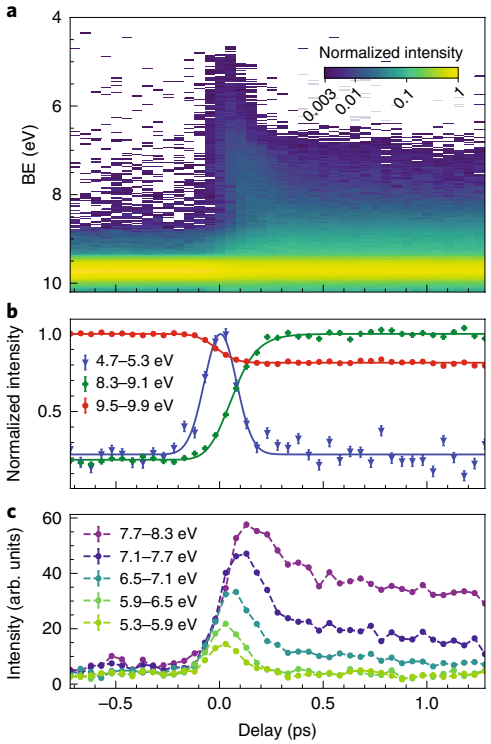

Fig. 2 | Time-dependent photoelectron spectra of UV-excited thiophenone. a, Measured photoelectron yield as a function of BE and time delay (Δt) between pump and probe pulses (see Supplementary Fig. 2 for a plot over a wider range of signal intensities, binding energies and delays). Negative Δt corresponds to the FEL pulse preceding the UV pulse and positive Δt to the UV pulse preceding the FEL pulse, while the colour represents the normalized photoelectron intensity. Regions with an intensity below 0.003 are shown in white. **b**, Delay-dependent photoelectron yields for three BE ranges selected to illustrate the photoinduced depopulation of the S_0 state (red circles), population of the S_2 state (blue triangles) and the build-up of vibrationally excited $S_0^{\#}$ photoproducts (green crosses). **c**, Delay-dependent photoelectron yields five contiguous 0.6 eV-wide BE slices that inform on the evolution from photoexcited S_2 to internally excited $S_0^{\#}$ molecules. Statistical error bars are included but are generally smaller than the symbol size. The parameters of the least-square fits shown as solid lines in **b** are summarized in Supplementary Table 1, while the dashed lines in **c** just join the dots for better visibility. The data in **b** have been normalized such that the maximum value of the fit is at 1 for each curve, whereas the data in **c** are displayed on a common intensity scale.

the S_0 state of thiophenone, wherein the highest occupied molecular orbital (HOMO) is an out-of-plane π orbital largely localized on the sulfur atom, henceforth labelled n(S). At our chosen pump photon energy, thiophenone is predominantly excited to its S_2 state. At the XMS(4)-CASPT2(10/8) level of theory, the $S_0 \rightarrow S_2$ transition has $n(S)/\pi^*$ character, a calculated transition energy of 4.67 eV and an appreciable oscillator strength (0.036), reflecting the constructive overlap of the donating n(S) and accepting π^* orbitals. The $S_0 \rightarrow S_1$ transition (with a calculated energy of 4.20 eV), by contrast, is dark (the donating O-atom centered, lone pair n(O) orbital lies in the plane of the ring and is thus orthogonal to the accepting orbital; see Section 2.1 in the Supplementary Information). Different minimum energy conical intersections (MECIs) were located between the S_2, S_1 and S_0 states of thiophenone, as shown in Fig. 3a. All of these MECIs indicate a ring opening in the excited electronic state (that is, formation of a biradical), followed by geometrical relaxation—for example, twisting of the CH_2–S moiety out of the molecular plane and bending of the C–C=O moiety (see also Section 2.2 in the Supplementary Information).

To determine the possible connections between these critical structures and the relaxation pathways of thiophenone following UV photoexcitation, linear interpolations in internal coordinates (LIICs) were performed using XMS(4)-CASPT2(10/8) (see Computational details). Starting from the FC geometry, the LIICs smoothly connect the different critical points and confirm that photoexcited thiophenone (S_2) molecules can relax efficiently towards the S_0 state via the S_2/S_1 and S_1/S_0 seams of intersection in the C–S bond extension coordinate[28]. The energies of the low-lying D_0 and D_1 states of the thiophenone cation were also computed at selected geometries along the LIIC pathways (Fig. 3a, dashed lines). In the FC region, these states are characterized by removal of an electron from, respectively, the n(S) and n(O) lone pair orbitals. As Fig. 3a shows, the topographies of the various PESs of neutral thiophenone vary strongly along the LIIC pathways, but the energies of the D_0 and D_1 states of the cation show a smooth and very gradual increase. The energy differences (ΔE) between the D_1/D_0 and the S_2/S_1 potentials along the LIIC pathways (inset in Fig. 3a) increase dramatically from the FC point out to the S_1/S_0 MECI. The calculations allow assignment of the experimentally observed rapid increase in BE with increasing Δt to the ultrafast depopulation of the S_2 state and electronic deactivation to the S_0 state, resulting in highly vibrationally excited ground-state molecules. We note that the calculated ΔE values are consistently slightly lower than the experimental BE values. Such underestimation of (experimental) IP values by (X)MS-CASPT2 methods is well-known[30] and, in the present case, can also be related to the choice of basis set (see Section 2.2 of the Supplementary Information).

The fates of the photoexcited thiophenone molecules were further explored by running trajectory surface hopping (TSH) calculations from the photoprepared S_2 state at the SA(4)-CASSCF(10/8) level of theory. These results are detailed in Section 2 of the Supplementary Information, and only the main features of the dynamics are highlighted here. As expected from inspection of the LIIC pathways, the initial S_2 population rapidly decays to the S_1 state and population appears almost immediately on the S_0 PES, as shown in Fig. 3b. All population is transferred to the S_0 state within 350 fs of UV excitation. Figure 3c displays a swarm of 46 TSH trajectories that mimic the relaxation dynamics of the thiophenone wavepacket and demonstrate that the ultrafast deactivation from S_2 to S_1 to S_0 is driven by a ballistic ring-opening process. The trajectories start to spread after ~50 fs; most remain ring-opened upon becoming $S_0^{\#}$ molecules, but some readopt a (vibrationally hot) cyclic configuration.

The conclusions from the TSH calculations match well with the experimental time-resolved photoelectron yields for the BE ranges selected to span the predicted IP_{vert} values along the LIIC (Fig. 2b,c). The yield in the BE range corresponding to vertical ionization from the S_2 state (blue trace in Fig. 2b) shows a narrow transient signal, the width of which is largely determined by the instrument response function. With increasing Δt, this transient signal shifts to higher BE, broadens somewhat and gains a longer time tail (Fig. 2c). Recalling the inset in Fig. 3a, these observed changes are all consistent with the wavepacket evolving on the S_2 PES (sampled most cleanly by intensities at BE ≤ 5.5 eV) and subsequent non-adiabatic coupling with the S_1 state (which are sampled most efficiently in the 6 ≤ BE ≤ 7 eV range) and thence with the S_0 PES (which start to be sampled at BE ≥ 7 eV). Ionization of $S_0^{\#}$ molecules accounts for the tails in the transients for the higher energy BE slices in Fig. 2c; the build-up of $S_0^{\#}$ population (green crosses in Fig. 2b) plateaus at $\Delta t \geq 300$ fs. These comparisons serve to reinforce the interpretation, developed from considering the LIIC pathways (Fig. 3a), that the experimentally observed increase in BE is a signature of the ultrafast decay of thiophenone (S_2) molecules to high $S_0^{\#}$ levels.

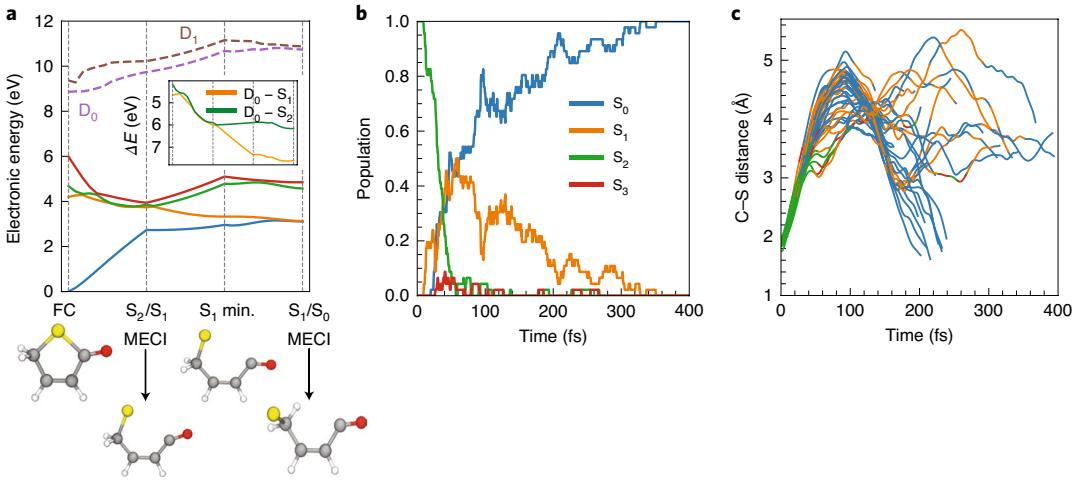

Fig. 3 | Ab initio calculations of PESs and excited-state dynamics. a, PESs for the lowest neutral singlet (solid lines; S_0 in blue, S_1 in orange, S_2 in green and S_3 in red) and cationic doublet (dashed lines) electronic states of thiophenone along LIIC pathways between different critical geometries. Electronic energies were obtained using XMS(4)-CASPT2(10/8) for the neutral and XMS(4)/CASPT2(9/8) for the cationic form of thiophenone. The critical geometries, minima and MECIs, located using the SA(4)-CASSCF(10/8) level of theory, are indicated with light-grey vertical lines, and the geometries of these critical points on the PESs of neutral thiophenone are shown below. LIIC pathways were then computed between each critical point, and the inset shows the electronic energy gap ΔE between the D_0 state of the cation and the second (S_2) or first (S_1) singlet states of neutral thiophenone for each point along the LIIC pathway. **b**, Time-dependence of the S_3, S_2, S_1 and S_0 state populations provided by the TSH dynamics (46 trajectories). **c**, Time-evolution of the C–S bond distance for each of these 46 trajectories, illustrating the prompt initial bond extension in all cases and (via the colour coding) the trajectory-dependent evolution from S_2 through S_1 to the S_0 state. The TSH trajectories were propagated until they experienced electronic structure instabilities in the ground state (see text).

Ground-state dynamics and reaction products. One key feature of the present experimental study is that the response of UV-excited thiophenone molecules can be followed not just en route to, but also after reaching, the S_0 PES. Figure 4a shows photoelectron spectra recorded at several pump–probe delays in the range $10 \leq \Delta t \leq 600$ ps. Most of the photoelectron intensity of interest at these large Δt values lies in the range $8.0 \leq \mathrm{BE} \leq 9.6$ eV, and the spectrum appears to consist of different contributions whose weights are Δt dependent; the intensity of the feature at lower BE (peaking at BE ≈ 8.8 eV) appears to increase relative to that of the feature peaking at BE ≈ 9.3 eV as Δt increases. To simulate the ground-state dynamics, the foregoing non-adiabatic molecular dynamics calculations using TSH in the lowest four electronic states were combined with ab initio molecular dynamics (AIMD, see Computational details) on the S_0 PES. From an electronic structure perspective, this required switching from an SA-CASSCF description (used for the excited-state dynamics) to an unrestricted density functional theory (UDFT) picture using the PBE0 exchange/correlation functional. The SA-CASSCF active space employed for the TSH dynamics became unstable when the trajectories were prolonged on the S_0 PES, but AIMD with UDFT was found to offer a stable alternative and allowed long-time simulation of the $S_0^{\#}$ species (see, for example, a previous study by Mignolet et al. [31]). Tests demonstrating the validity of this approach for the present system are reported in Supplementary Section 2.5.

To initiate the $S_0^{\#}$ molecular dynamics after passage through the S_1/S_0 seam of intersection, the AIMD trajectories were launched from the nuclear coordinates and with the momenta extracted from the TSH trajectories after the S_0 state had been reached. Thus, the present AIMD simulations are not per se in a ground-state thermal equilibrium, since the internal energy of the molecule at the start of the S_0-state dynamics calculation depends on the history of the TSH trajectory in the excited state; that is, the approach allows description of non-statistical effects in the hot S_0-state dynamics. In total, 22 AIMD trajectories were propagated until $t = 2$ ps and, to explore the longer-time dynamics, 10 of these were propagated further to $t = 100$ ps (see Computational details and Section 2.10 in the Supplementary Information). Since each is a continuation of an excited-state trajectory, the starting configuration in each case involves a ring-opened or highly stretched molecule.

The AIMD simulations reveal formation of several different photoproducts within the earliest timescales of these dynamics. Ring closure (resulting in re-formation of hot thiophenone molecules) is observed, as is the formation of the acyclic isomers 2-thioxoethylketene (P1), 2-(2-sulfanylethyl)ketene (P2) and 2-(2-thiiranyl)ketene (P3) (see Fig. 4b for structures). Interconversion between these isomers was observed in most trajectories within 2 ps (see Supplementary Fig. 12). The histogram labelled 'other' in Fig. 4b includes all molecular geometries that could not be attributed to P1, P2, P3 or closed-ring thiophenone products. These rare other geometries often correspond to transient configurations in the act of interconverting between the dominant photoproducts and are mostly observed within 500 fs of accessing the S_0-state PES. It is important to emphasize that these AIMD calculations (and the gas-phase experiments) involve isolated molecules. The potential energy acquired by thiophenone upon photoexcitation is converted, in part, to nuclear kinetic energy during the non-radiative decay to the S_0 state, but these are closed systems: no energy dissipation is possible and the resulting $S_0^{\#}$ species are highly energetic.

Experimentally, the BEs of the $S_0^{\#}$ species formed via non-radiative de-excitation are concentrated in a narrow (~1 eV, full width at half maximum (FWHM)) band centred at ~9 eV, as shown in Figs. 4a,c. Yet the AIMD simulations indicate that this ensemble of $S_0^{\#}$ species must contain a range of structures with high internal energies. Thus, the 22 AIMD outputs were analysed further. Specifically, the molecular geometry was extracted every 10 fs from each AIMD trajectory, yielding a pool of >4,000 geometries. These were grouped by photoproduct (see Section 2.6 in the Supplementary Information) and, for each geometry, the IP_{vert} value between the S_0 and D_0 states was calculated using MP2-F12/cc-pVDZ-F12 to provide an estimate of the BE. As Fig. 4b shows, the histograms of the IP_{vert} values for

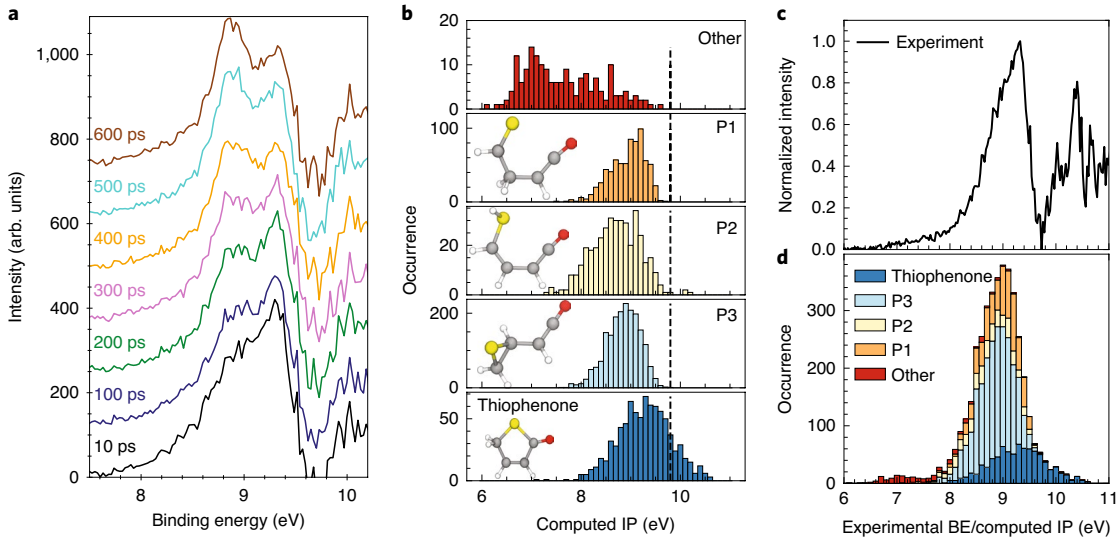

Fig. 4 | Dynamics on the S_0 PES following photoexcitation and non-radiative decay. a, Photoelectron spectra for different pump–probe delays after subtraction of the signal from 'unpumped' thiophenone (S_0) molecules (see Supplementary Fig. 3 for details). The spectra are offset vertically for better visibility. **b**, Histograms showing the number of occurrences of the various $S_0 \rightarrow D_0$ IP_{vert} values computed at the MP2/cc-pVDZ-F12 level of theory every 10 fs (for a total of 2 ps) along each AIMD trajectory on the S_0 PES, grouped by similarity to the molecular geometries identified as P1, P2, P3 and closed-ring thiophenone, along with a further small group labelled 'other' associated with internally hot molecules that were in the act of converting between stable isomeric forms at the time the trajectory was sampled (see text). The calculated IP_{vert} for thiophenone at its optimized ground-state geometry is indicated by a dashed vertical black line. **c**, Experimental (subtracted) photoelectron spectrum summed over the delay range $0.5 \leq \Delta t \leq 2$ ps; the contribution at BE > 9.8 eV is due to ionization of $S_0^{\#}$ molecules to excited cationic states, which are not included in the present calculations (see also Supplementary Figs. 2, 3 and 15). **d**, Sum of the five distributions of IP_{vert} values shown in **b**.

each photoproduct span a narrow range, and the ground-state photoproducts P1, P2 and P3 display similar IP_{vert} distributions. This reflects the fact that, in each case, ionization involves removal of an electron from an orbital with a high degree of *n*(S) character. The distribution associated with re-formed closed-ring thiophenone species is centred at slightly higher IP_{vert} values. For completeness, we note that the predicted distribution of $S_0 \rightarrow D_0$ IP_{vert} values for thiophenone molecules without the extra kinetic energy induced by photoexcitation and subsequent relaxation (derived from AIMD simulations of thiophenone initiated with an internal energy equal to the zero-point energy only) is centred at yet higher IP_{vert}, is much narrower and, as Supplementary Fig. 15 shows, is in very good accord with the lowest energy peak in the measured He I photoelectron spectrum[29].

Returning to the hot $S_0^{\#}$ molecules, the 22 AIMD outputs predict a narrow overall distribution of IP_{vert} values (Fig. 4d) that, as Fig. 4c shows, matches well with the TRPES data summed over the delay range $0.5 \leq \Delta t \leq 2$ ps. The 10 AIMD outputs propagated to $t = 100$ ps (see Supplementary Fig. 17) provide additional insights into the longer-time dynamics of these $S_0^{\#}$ molecules. Analysis of the (admittedly small number of) long-time trajectories reveals (1) irreversible conversion of closed-ring to open-ring isomers and (2), in several cases, unimolecular decay of the $S_0^{\#}$ species to CO + thioacrolein ($CH_2CHC(H)S$) products. The first IP_{vert} of thioacrolein is 8.9 eV (see a study by Bock et al.[32]), a value reproduced computationally in the present work (see Section 2.10 in the Supplementary Information). Thus, recalling Fig. 4b, we note that all closed-ring to open-ring transformations (including the fragmentation process) will cause a net transfer of $S_0^{\#}$ population to species with lower IP_{vert} (that is, lower BE) values—consistent with the experimental observations (Fig. 4a).

Conclusions

A previous transient infrared absorption spectroscopy study of the UV photoexcitation of thiophenone in solution (that is, in an environment where any product vibrational excitation is rapidly dissipated through interaction with the solvent)[18] demonstrated the formation of acyclic photoproduct(s) with ketene structures and the recovery of (vibrationally cold) ground-state thiophenone molecules. These earlier studies lacked the temporal resolution to probe the ring-opening mechanism directly, and the only $S_0^{\#}$ dynamics amenable to investigation were vibrational relaxation dynamics via interaction with the solvent molecules. Such limitations are not an issue in this study, wherein time-resolved XUV photoelectron spectroscopy studies of the isolated (gas-phase) molecules at a seeded FEL, in combination with high-level ab initio theory, have enabled detailed visualization of the electronic and, particularly, the structural dynamics of this complex photoinduced ring-opening reaction. We have revealed the initial motion following photoexcitation, the non-adiabatic coupling to the S_0 PES as an open-ring biradical, and the subsequent isomerizations and eventual decay of the highly vibrationally excited S_0-state species. The match between theory and experiment spans both the excited-state decay rates and the more challenging athermal rearrangements to photoproducts that occur after non-adiabatic coupling to the S_0 state.

The use of sufficiently high-energy probe photons is key to tracking the full decay dynamics, that is, the ultrafast evolution of the photoexcited wavepacket to the S_0 state and the nuclear dynamics of the resulting highly vibrationally excited S_0 molecules. The increase in BE observed immediately post-photoexcitation is a signature of the ultrafast decay of the nuclear wavepacket from the S_2 state, via the S_1 state, towards the electronic ground state, enabled by elongation and eventual scission of the S–CO bond. The evolving molecules couple to the S_0 PES with a range of geometries and nuclear momenta, which govern the subsequent athermal rearrangements of the $S_0^{\#}$ species. These vibrationally excited S_0 molecules are highly fluxional and can adopt at least three identified open-ring structures or re-form the parent thiophenone, and they have sufficient internal energy to dissociate (by loss of a CO moiety). The deduced ground-state dynamics serve to bolster a recent

prediction that isomerization of energized molecules prior to dissociation might well be the rule rather than the exception in many polyatomic unimolecular processes[33]. The IP_{vert} distribution computed from the AIMD trajectories on the S_0 PES reproduces the narrow spread of BEs observed experimentally and can be traced to the localized nature of the sulfur lone pair orbital that is the dominant contributor to the HOMO in each species. Distinguishing the various open-ring products by valence-shell photoelectron spectroscopy is challenging given their very similar first IPs. Ultrafast X-ray or electron diffraction studies might be able to address such structural challenges if sufficient scattering signal can be obtained despite the low sample vapour pressure.

Online content

Any Nature Research reporting summaries, source data, extended data, supplementary information, acknowledgements, peer review information; details of author contributions and competing interests; and statements of data and code availability are available at https://doi.org/10.1038/s41557-020-0507-3.

Received: 10 November 2019; Accepted: 11 June 2020;
Published online: 20 July 2020

References

1. Minitti, M. P. et al. Imaging molecular motion: Femtosecond X-Ray scattering of the ring opening in 1,3-cyclohexadiene. *Phys. Rev. Lett.* **114**, 255501 (2015).
2. Pullen, M. G. et al. Imaging an aligned polyatomic molecule with laser-induced electron diffraction. *Nat. Commun.* **6**, 7262 (2015).
3. Wolter, B. et al. Ultrafast electron diffraction imaging of bond breaking in di-ionized acetylene. *Science* **354**, 308–312 (2016).
4. Attar, A. R. et al. Femtosecond X-ray spectroscopy of an electrocyclic ring-opening reaction. *Science* **356**, 54–59 (2017).
5. Schuurman, M. S. & Stolow, A. Dynamics at conical intersections. *Annu. Rev. Phys. Chem.* **69**, 427–450 (2018).
6. Wolf, T. J. A. et al. The photochemical ring-opening of 1,3-cyclohexadiene imaged by ultrafast electron diffraction. *Nat. Chem.* **11**, 504–509 (2019).
7. Ruddock, J. M. et al. A deep UV trigger for ground-state ring-opening dynamics of 1,3-cyclohexadiene. *Sci. Adv.* **5**, eaax6625 (2019).
8. Stankus, B. et al. Ultrafast X-ray scattering reveals vibrational coherence following Rydberg excitation. *Nat. Chem.* **11**, 716–721 (2019).
9. Browne, W. R. & Feringa, B. L. Light switching of molecules on surfaces. *Annu. Rev. Phys. Chem.* **60**, 407–428 (2009).
10. Kumpulainen, T., Lang, B., Rosspeintner, A. & Vauthey, E. Ultrafast elementary photochemical processes of organic molecules in liquid solution. *Chem. Rev.* **117**, 10826–10939 (2017).
11. Qi, J. et al. Light-driven transformable optical agent with adaptive functions for boosting cancer surgery outcomes. *Nat. Commun.* **9**, 1848 (2018).
12. Deb, S. & Weber, P. M. The ultrafast pathway of photon-induced electrocyclic ring-opening reactions: The case of 1,3-cyclohexadiene. *Annu. Rev. Phys. Chem.* **62**, 19–39 (2011).
13. Arruda, B. C. & Sension, R. J. Ultrafast polyene dynamics: the ring opening of 1,3-cyclohexadiene derivatives. *Phys. Chem. Chem. Phys.* **16**, 4439–4455 (2014).
14. Petrović, V. S. et al. Transient X-ray fragmentation: Probing a prototypical photoinduced ring opening. *Phys. Rev. Lett.* **108**, 253006 (2012).
15. Rudakov, F. & Weber, P. M. Ground state recovery and molecular structure upon ultrafast transition through conical intersections in cyclic dienes. *Chem. Phys. Lett.* **470**, 187–190 (2009).
16. Adachi, S., Sato, M. & Suzuki, T. Direct observation of ground-state product formation in a 1,3-cyclohexadiene ring-opening reaction. *J. Phys. Chem. Lett.* **6**, 343–346 (2015).
17. Breda, S., Reva, I. & Fausto, R. UV-induced unimolecular photochemistry of 2(5H)-furanone and 2(5H)-thiophenone isolated in low temperature inert matrices. *Vib. Spectrosc.* **50**, 57–67 (2009).
18. Murdock, D. et al. Transient UV pump–IR probe investigation of heterocyclic ring-opening dynamics in the solution phase: the role played by nσ* states in the photoinduced reactions of thiophenone and furanone. *Phys. Chem. Chem. Phys.* **16**, 21271–21279 (2014).
19. Allaria, E. et al. Highly coherent and stable pulses from the FERMI seeded free-electron laser in the extreme ultraviolet. *Nat. Photonics* **6**, 699–704 (2012).
20. Stolow, A., Bragg, A. E. & Neumark, D. M. Femtosecond time-resolved photoelectron spectroscopy. *Chem. Rev.* **104**, 1719–1757 (2004).
21. Suzuki, T. Time-resolved photoelectron spectroscopy of non-adiabatic electronic dynamics in gas and liquid phases. *Int. Rev. Phys. Chem* **31**, 265–318 (2012).
22. Iikubo, R., Sekikawa, T., Harabuchi, Y. & Taketsugu, T. Structural dynamics of photochemical reactions probed by time-resolved photoelectron spectroscopy using high harmonic pulses. *Faraday Discuss.* **194**, 147–160 (2016).
23. Nishitani, J., West, C. W., Higashimura, C. & Suzuki, T. Time-resolved photoelectron spectroscopy of polyatomic molecules using 42-nm vacuum ultraviolet laser based on high harmonics generation. *Chem. Phys. Lett.* **684**, 397–401 (2017).
24. Smith, A. D. et al. Mapping the complete reaction path of a complex photochemical reaction. *Phys. Rev. Lett.* **120**, 183003 (2018).
25. von Conta, A. et al. Conical-intersection dynamics and ground-state chemistry probed by extreme-ultraviolet time-resolved photoelectron spectroscopy. *Nat. Commun.* **9**, 3162 (2018).
26. Squibb, R. J. et al. Acetylacetone photodynamics at a seeded free-electron laser. *Nat. Commun.* **9**, 63 (2018).
27. Gorobtsov, O. Y. et al. Seeded X-ray free-electron laser generating radiation with laser statistical properties. *Nat. Commun.* **9**, 4498 (2018).
28. Xie, B.-B. & Fang, W.-H. Combined quantum trajectory mean-field and molecular mechanical (QTMF/MM) nonadiabatic dynamics simulations on the photoinduced ring-opening reaction of 2(5H)-thiophenone. *ChemPhotoChem* **3**, 897–906 (2019).
29. Chin, W. S. et al. He I and He II photoelectron spectra of thiophenones. *J. Electron Spectrosc. Relat. Phenomena* **88-91**, 97–101 (1998).
30. Tao, H. et al. Ultrafast internal conversion in ethylene. I. The excited state lifetime. *J. Chem. Phys.* **134**, 244306 (2011).
31. Mignolet, B., Curchod, B. F. E. & Martínez, T. J. Rich athermal ground-state chemistry triggered by dynamics through a conical intersection. *Angew. Chem. Int. Ed. Engl.* **55**, 14993–14996 (2016).
32. Bock, H., Mohmand, S., Hirabayashi, T. & Semkow, A. Gas-phase reactions. 29. Thioacrolein. *J. Am. Chem. Soc.* **104**, 312–313 (1982).
33. Yang, C.-S., Bhattacharyya, S., Liu, L., Fang, W.-H. & Liu, K. Real-time tracking of the entangled pathways in the multichannel photodissociation of acetaldehyde. *Chem. Sci*. https://doi.org/10.1039/d0sc00063a (2020).

Publisher's note Springer Nature remains neutral with regard to jurisdictional claims in published maps and institutional affiliations.

© The Author(s), under exclusive licence to Springer Nature Limited 2020

Methods

Experimental. The experiment was performed at the low-density matter (LDM) beamline[34,35] at the FERMI free-electron laser facility[19]. The FEL was operated at a photon energy of 19.24 eV, corresponding to the fourth harmonic of the seed laser, with an estimated pulse duration of 80 fs (FWHM)[36]. The UV pump pulses, with a centre wavelength of 264.75 nm and a 1.2 nm bandwidth, were generated as the third harmonic of a Ti:Sapphire laser. Details relating to gas sample delivery, other laser pulse parameters (energies, durations and spot sizes) and tests to ensure that the reported effects scale linearly with pump and probe pulse parameters are reported in Section 1 of the Supplementary Information. A magnetic bottle type spectrometer[26,37] (see Supplementary Fig. 1) was used to detect photoelectrons with high collection efficiency. A retardation voltage of 8 V was used to increase the resolution in the photoelectron range of interest (the approximate kinetic energy resolution is $\delta E/E \approx 0.03$, with E being the final kinetic energy after retardation), cutting off the photoelectron spectrum at a binding energy of approximately 11 eV, as shown in Supplementary Fig. 2.

Data acquisition and analysis. Time-of-flight traces were recorded shot-by-shot while scanning the delay between the pump and probe pulses. The data shown in Fig. 1a consist of ~1,650 shots per 50 fs delay bin. The single-shot spectra were summed for each delay bin and then normalized with respect to the summed FEL intensity (measured shot-to-shot[38]). The electron time-of-flight was converted into photoelectron kinetic energy by calibrating the spectrometer using photoelectrons from the single-photon single ionization of helium at multiple harmonics (that is, different photon energies) of the FEL. The photoelectron energies were then converted to binding energies by subtracting the photoelectron energy from the FEL photon energy.

Computational details. *Critical points and linear interpolation in internal coordinates.* Critical points of the thiophenone PESs—S_0 minimum, S_1 minima, and S_2/S_1 and S_1/S_0 MECIs—were located using SA(4)-CASSCF(10/8)[39,40] and a 6-31G* basis set[41,42] as implemented in Molpro 2012[43]. Pathways connecting these different critical points of the PESs were produced by LIICs[44]. Some of the advantages and limitations of LIICs are summarized in Section 2.2 in the Supplementary Information. Electronic energies for thiophenone were computed along the LIIC pathways at the SA(4)-CASSCF(10/8) and XMS(4)-CASPT2(10/8)[45,46] levels of theory using, in all cases, a 6-31G* basis set (see Supplementary Figs. 7 and 8). The electronic energies for the thiophenone cation were also computed along the LIICs using SA(4)-CASSCF(9/8) and XMS(4)-CASPT2(9/8). All XMS-CASPT2 calculations were performed with the BAGEL software[47], employing the corresponding SA-CASSCF wavefunction from Molpro 2012 as a starting point. A level shift[48] of 0.3 E_h was used in all XMS-CASPT2 calculations to prevent the appearance of intruder states. For details on the calculations of IPs, including benchmarking studies justifying this choice of basis set, see Section 2 in the Supplementary Information.

TSH dynamics. The excited-state dynamics of thiophenone following photoexcitation were simulated using the mixed quantum/classical dynamics TSH method, employing the fewest-switches algorithm[49]. All details regarding these dynamics are provided in Section 2 of the Supplementary Information.

Ab initio molecular dynamics to $t = 2$ ps and $t = 100$ ps. AIMD calculations of the photoproducts formed during the TSH dynamics were conducted on the S_0-state PES using unrestricted DFT with the PBE0 exchange/correlation functional[50] and a 6-31G* basis set, employing the GPU-accelerated software TeraChem[51]. The initial conditions (nuclear coordinates and velocities) for each AIMD trajectory (22 in total, drawn randomly from the pool of TSH trajectories) were extracted from the TSH dynamics when the trajectory reached the S_0 state. At this initial point in configuration space, the SA-CASSCF wavefunction already exhibits a dominant closed-shell character (confirmed at the XMS-CASPT2 level of theory; see Section 2.5 in the Supplementary Information for additional details). A small (0.1 fs) time step was used to ensure proper total energy conservation for all trajectories, and the length of each (constant total energy) trajectory was set such that the total TSH + AIMD dynamics extend to 2 ps. This strategy necessarily restricts the dynamics to the S_0 PES; the legitimacy of this procedure was validated by test trajectories on S_0, which show the energy separation between the ground and excited electronic states increasing rapidly upon leaving the region of the S_1/S_0 seam of intersection. To explore the long-time dynamics of the different photoproducts, 10 of the 22 trajectories were propagated further, to $t = 100$ ps, using the same methodology except for a slightly longer time step of 0.25 fs.

Analysis of the 2 ps AIMD and vertical ionization energy distribution. The 22 AIMD trajectories propagated until $t = 2$ ps were used to analyse the distribution of IP_{vert} values for the $S_0^{\#}$ photoproducts. For each AIMD trajectory, molecular geometries were sampled every 10 fs, leading to a pool of >4,000 S_0 molecular configurations. Each configuration was assigned to one of the possible photoproducts identified by Murdock et al.[18] based on characteristic atomic connectivities determined by measuring bond lengths or angles (see Supplementary Fig. 13). If such assignment was not possible, the configuration was given the label 'others'. These were often due to a transient configuration between two photoproducts. The IP_{vert} of each configuration was then computed at the MP2-F12/cc-pVDZ-F12 level of theory (this level of theory was benchmarked against CCSD(T)-F12/cc-pVDZ-F12; see Section 2.8 in the Supplementary Information). The resulting distribution of $S_0 \rightarrow D_0$ IP_{vert} values provides an approximation of the low-energy part of the experimental BE spectra. The same methodology, applied to ground-state dynamics of cold thiophenone, successfully reproduces the first peak in the experimental He I photoelectron spectrum (see Supplementary Fig. 15). All calculations were performed with Molpro 2012.

Data availability

Data generated or analysed during this study are included in this Article (and its Supplementary Information). Source data are provided with this paper.

Code availability

The analysis codes used to generate the data presented in this study are available from the corresponding authors upon reasonable request. Source data are provided with this paper.

References

34. Svetina, C. et al. The low density matter (LDM) beamline at FERMI: optical layout and first commissioning. *J. Synchrotron Radiat.* **22**, 538–543 (2015).
35. Lyamayev, V. et al. A modular end-station for atomic, molecular, and cluster science at the low density matter beamline of FERMI@Elettra. *J. Phys. B* **46**, 164007 (2013).
36. Finetti, P. et al. Pulse duration of seeded free-electron lasers. *Phys. Rev. X* **7**, 021043 (2017).
37. Eland, J. H. D. et al. Complete two-electron spectra in double photoionization: the rare gases Ar, Kr, and Xe. *Phys. Rev. Lett.* **90**, 053003 (2003).
38. Zangrando, M. et al. Recent results of PADReS, the photon analysis delivery and reduction system, from the FERMI FEL commissioning and user operations. *J. Synchrotron Radiat.* **22**, 565–570 (2015).
39. Werner, H.-J. in *Advances in Chemical Physics: Ab Initio Methods in Quantum Chemistry Part 2* Vol. 69 (ed. Lawley, K. P.) Ch. 1 (Wiley, 1987).
40. Roos, B. O. in *Advances in Chemical Physics: Ab Initio Methods in Quantum Chemistry Part 2* Vol. 69 (ed. Lawley, K. P.) Ch. 7 (Wiley, 1987).
41. Hehre, W. J., Ditchfield, R. & Pople, J. A. Self-consistent molecular orbital methods. XII. Further extensions of Gaussian-type basis sets for use in molecular-orbital studies of organic-molecules. *J. Chem. Phys.* **56**, 2257–2261 (1972).
42. Hariharan, P. C. & Pople, J. A. Influence of polarization functions on molecular-orbital hydrogenation energies. *Theor. Chem. Acc.* **28**, 213–222 (1973).
43. Werner, H.-J. et al. MOLPRO, v.2012.1 (Molpro, 2012); https://www.molpro.net
44. Hudock, H. R. et al. Ab initio molecular dynamics and time-resolved photoelectron spectroscopy of electronically excited uracil and thymine. *J. Phys. Chem. A* **111**, 8500–8508 (2007).
45. Shiozaki, T., Győrffyet, W., Celani, C. & Werner, H.-J. Communication: Extended multi-state complete active space second-order perturbation theory: Energy and nuclear gradients. *J. Chem. Phys.* **135**, 081106 (2011).
46. Granovsky, A. Extended multi-configuration quasi-degenerate perturbation theory: The new approach to multi-state multi-reference perturbation theory. *J. Chem. Phys.* **134**, 214113 (2011).
47. BAGEL Brilliantly Advanced General Electronic-Structure Library v.1.2.2 (Shiozaki Group, 2018); http://www.nubakery.org
48. Ghigo, G., Roos, B. O. & Malmqvist, P. A. A modified definition of the zeroth-order Hamiltonian in multiconfigurational perturbation theory (CASPT2). *Chem. Phys. Lett.* **396**, 142–149 (2004).
49. Tully, J. C. Molecular dynamics with electronic transitions. *J. Chem. Phys.* **93**, 1061–1071 (1990).
50. Adamo, C. & Barone, V. Toward reliable density functional methods without adjustable parameters: The PBE0 model. *J. Chem. Phys.* **110**, 6158–6169 (1999).
51. Ufimtsev, I. S. & Martínez, T. J. Quantum chemistry on graphical processing units. 3. analytical energy gradients, geometry optimization, and first principles molecular dynamics. *J. Chem. Theory Comput.* **5**, 2619–2628 (2009).

Acknowledgements

S.P., J.T. and D.R. were supported by the National Science Foundation (NSF) grant PHYS-1753324. S.P. was also partially supported by the Chemical Sciences, Geosciences, and Biosciences Division, Office of Basic Energy Sciences, Office of Science, US Department of Energy (DOE) under grant no. DE-FG02-86ER13491. Travel to FERMI for S.P., D.M.P.H., R.M., J.T. and D.R. was supported by LaserLab Europe. This work made use of the facilities of the Hamilton HPC Service of Durham University. M.N.R.A., C.S.H. and R.A.I. acknowledge the Engineering and Physical Sciences Research Council (EPSRC) for funding (EP/L005913/1), while L.M.I. acknowledges the EPSRC for a doctoral

studentship (EP/R513039/1). C.S.H. also acknowledges funding from the Australian Research Council (ARC, DE200100549). M.N.R.A. thanks W.-H. Fang (Beijing Normal University) for permission to share data[28] prior to its publication. B.F.E.C. acknowledges funding from the European Union Horizon 2020 research and innovation programme under grant agreement no. 803718 (SINDAM). D.M.P.H. was supported by the Science and Technology Facilities Council, UK. R.F. and R.J.S. acknowledge financial support from the Swedish Research Council, the Knut and Alice Wallenberg Foundation, Sweden, and the Faculty of Natural Science of the University of Gothenburg. We thank the technical and scientific teams at FERMI for their hospitality and their support during the beamtime. We also acknowledge helpful discussions with A. Rudenko during the preparation of the beamtime proposal and during the data interpretation and with S. Bhattacharyya during the data analysis and interpretation.

Author contributions

R.B., R.A.I., C.S.H., M.N.R.A. and D.R. conceived the experiment, the plans for which benefitted from further input from R. Forbes, D.M.P.H. and A.R. The experiment was conducted by S.P., R.A.I., R.B., C.C., A.D., B.E., R. Feifel, M.D.F., L.G., C.S.H., D.M.P.H., R.M., O.P., K.C.P., A.R., R.J.S., J.T., M.N.R.A. and D.R. at the FERMI free-electron laser facility. R. Feifel and R.J.S. provided and operated the magnetic bottle spectrometer. C.C., M.D.F. and O.P. prepared and operated the beamline and the low-density matter (LDM) instrument. A.D. and L.G. prepared and operated the optical laser and the free-electron laser, respectively. L.M.I. and B.F.E.C. performed the ab initio simulations, with contributions from R.A.I. Experimental data were analysed by S.P. and J.T. with contributions from C.C., R. Forbes, C.S.H., R.A.I., R.M. and A.R. Finally, S.P., L.M.I., R.B., R. Forbes, M.N.R.A., B.F.E.C. and D.R. interpreted the results and wrote the manuscript with input from all the authors.

Competing interests

The authors declare no competing interests.

Additional information

Supplementary information is available for this paper at https://doi.org/10.1038/s41557-020-0507-3.

Correspondence and requests for materials should be addressed to M.N.R.A., B.F.E.C. or D.R.

Reprints and permissions information is available at www.nature.com/reprints.